





Research Article

Microstructure Evolution and Multiscale Heat Transfer Characteristics of Resin-Based Ablative Material under Aerodynamic Heating

Junjie Gao ^{1,2}, Daiying Deng ^{1,2}, Haitao Han ^{1,2} and Jijun Yu ^{1,2}

¹China Academy of Aerospace Aerodynamics, Beijing 100074, China

²Laboratory of Aero-Thermal Protection Technology for Aerospace Vehicles, China Aerospace Science and Technology, Beijing 100074, China

Correspondence should be addressed to Junjie Gao; gao58_jj@163.com

Received 25 February 2023; Revised 18 July 2023; Accepted 5 September 2023; Published 16 October 2023

Academic Editor: Mohammad Tawfik

Copyright © 2023 Junjie Gao et al. This is an open access article distributed under the Creative Commons Attribution License, which permits unrestricted use, distribution, and reproduction in any medium, provided the original work is properly cited.

This paper is aimed at investigating the microstructure evolution of resin-based ablative materials under aerodynamic heating. The microstructure, morphology, material density, and thermophysical parameters at different positions of the material after aerodynamic heating were deeply studied. The changes in the microstructural characteristics of materials caused by complex reaction processes were investigated, including microstructural morphology, porosity, the overlap relationship between microstructural components, and the mutual positional relationship. The relationship between microstructural evolution and material heat transfer is discussed. By analyzing the heat transfer mechanism and heat transfer path of the microstructure, combining with the analysis results of the evolution of the microstructure and the physical properties of the material, multiscale heat transfer unit cell models were established to predict the equivalent thermal conductivity. Thereby, the evolution of physical properties and microstructure of resin-based ablative materials under aerodynamic heating and the relationship between microstructure evolution and heat transfer process are obtained. It can improve the accuracy of ablative heat transfer simulation. In addition, it can provide reference for the process design of ablative materials and promote the application and development of ablative materials in the field of aircraft.

1. Introduction

Since the 1960s, the thermal barrier problem of reentry vehicles has become a hindrance to the development of hypersonic vehicles. So, aerothermal protection technology has become a hot topic in aerothermodynamic research. Ablative thermal protection technology has overcome the difficult thermal barrier problem which is difficult to be solved by a single discipline in a short time [1]. The resin-based ablative material has been widely used because of its high heat protection efficiency, good reliability, and simple structure. The first application of ablative materials was the phenolic-based composite used on the MK3 warhead of the Hercules I missile in the middle 1950s [2].

Ablative materials will produce a series of physical and chemical reactions in the aerodynamic heating environment (i.e., melting, pyrolysis, ejection of pyrolytic gas into the boundary layer, sublimation, and in-phase and out-phase chemical reactions). During these physical and chemical reactions, ablative materials are consumed, and the heat given by the environment is dissipated in different ways. This way, the internal structure of the vehicle works at the permitted temperature [3].

For the long-time reentry capsule of the manned spacecraft and the reentry satellite with medium and low thermal flow, lightweight resin-based ablative materials with heat-proof and heat-insulating properties are usually used [4]. For example, the Avcoat 5026-39G was used on the Apollo

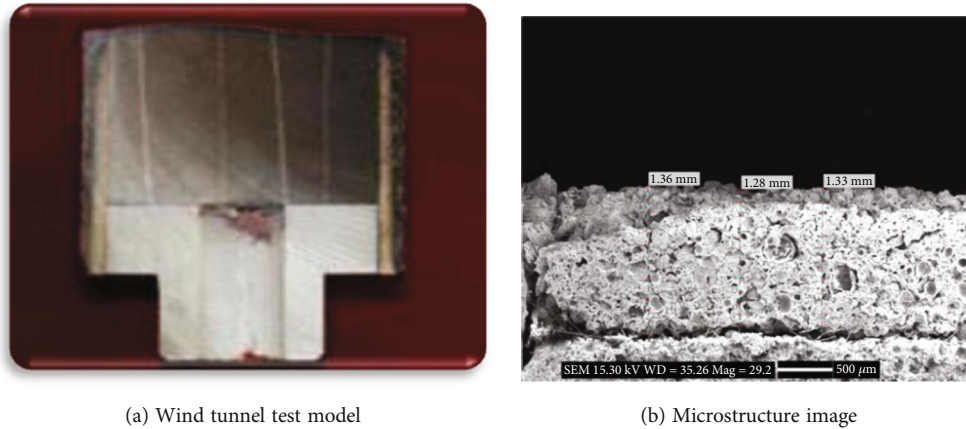


FIGURE 1: The wind tunnel test model and microstructure image of H96 material after aerodynamic heating.

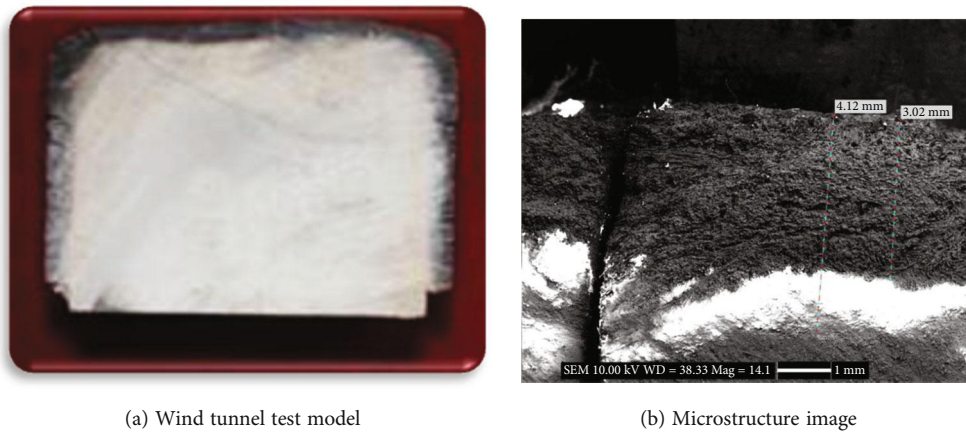


FIGURE 2: The wind tunnel test model and microstructure image of H96-modified material after aerodynamic heating.

spacecraft; it is made of phenolic glass honeycomb cells filled with phenolic epoxy resin, quartz fibers, and phenolic pellets. The Shenzhou spacecraft used H88 and H96 materials (as shown in Figures 1 and 2); it is phenolic glass honeycomb lattice filled with silicone rubber.

The Lee area of the US Mars reentry vehicle (Viking, Pathfinder) uses lightweight ablative materials made of cork powder, silicone, and phenolic resin microspheres. During the ablative process, resin pyrolysis and carbonization, pyrolytic gas ejection, surface oxidation, and other chemical reactions occur, which can significantly reduce the effective heat flow into the thermal shield. At the same time, the strong thermal insulation performance can ensure the internal temperature of the spacecraft structure to be within the allowable range.

In order to explore the performance of heat protection and heat insulation, thermochemical ablative and heat transfer theory are used. With the wind tunnel and flight test data, the ablative and heat transfer simulation methods of typical resin-based thermal protection materials were established. It can give relatively accurate prediction results of ablation and heat transfer response and make contribution to the success of reentry vehicle. With the development of

reentry vehicles, the limits of the proportion of ablative material become increasingly strict. So, it put forward higher requirements of the precision of ablative and heat transfer response of resin-based ablative material. We need to explore the ablative and heat transfer response at the mesoscopic and microscopic scale. In the mesoscopic scale, mainly in the micron scale, the ablative morphology of the material and the mechanism of the ablation were studied. The microlevel mainly refers to the analysis at the nanoscale.

The microstructure of the composite material was studied mainly by scanning electron microscope, transmission electron microscope, X-ray diffractometer, Raman spectroscopy, and other experimental methods.

For phenolic resin materials, phenolic resin-based carbon-carbon composites, and pyrolytic short fiber-reinforced polymer resin matrix composites, Ko et al. [5], Tzeng and Chr [6] (as shown in Figure 3), and Alex et al. [7] studied the microstructure of pyrolyzed materials at different temperatures by means of Raman spectroscopy, X-ray diffractometer, and scanning electron microscope separately. For polymer-derived silicon carbide ceramic composites, Santhosh et al. [8] studied the effects of pyrolysis temperature on the microstructure and thermal conductivity of

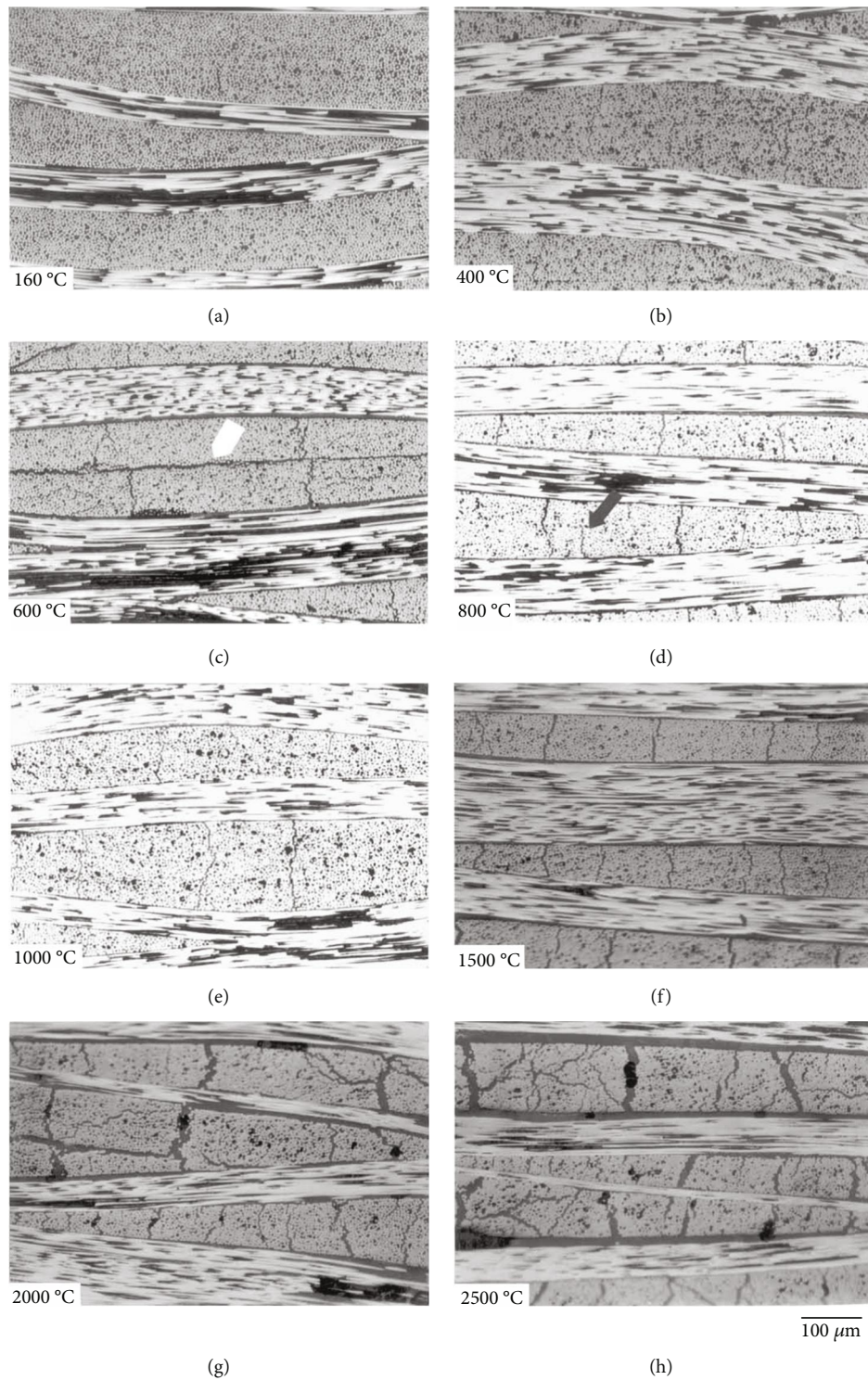


FIGURE 3: Pyrolytic microstructure of resin-based carbon-carbon composites at different temperatures: (a) 160°C, (b) 400°C, (c) 600°C, (d) 800°C, (e) 1000°C, (f) 1500°C, (g) 2000°C, and (h) 2500°C [6].

polymer-derived silicon carbide ceramic composites by TG, FT-IR, TEM, and SEM. In recent years, the influence of different processes on the microstructure during the production of composite materials has been explored, including three-dimensional carbon fiber-reinforced ceramic matrix composites [9] (as shown in Figure 4), ceramic hollow

microsphere composites [10], carbon-mullite composites [11], and silicon carbide ceramic composites [12].

Most of the previous studies were conducted to test and analyze the influence of different pyrolysis temperatures on the microstructure of materials and to explore the evolution of the microstructure of materials under different

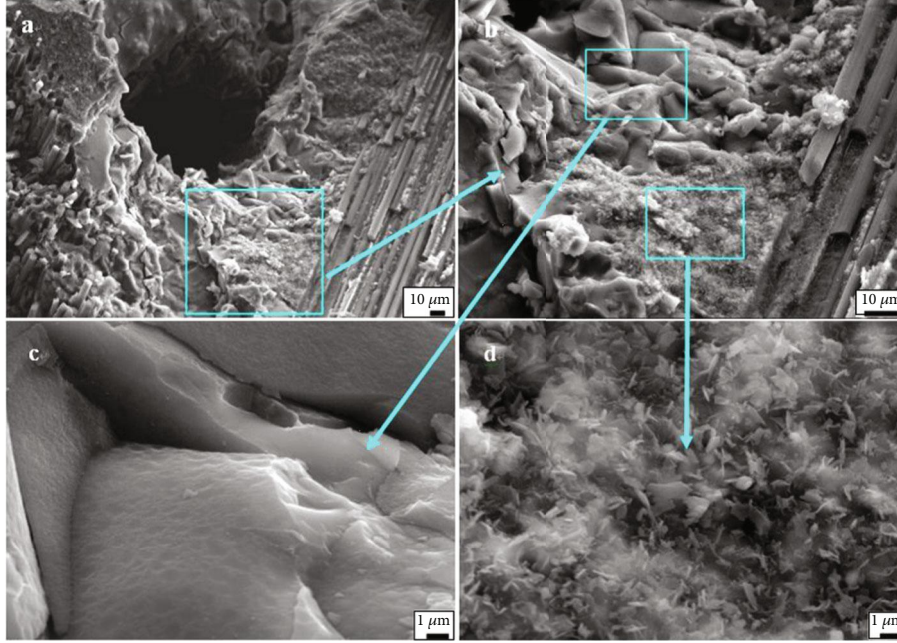


FIGURE 4: Microstructure of fiber bundle region and matrix surrounding the pore in three-dimensional Cf/SiC-BN composites [9].

technological processes. However, there are still few researches on the microstructure evolution of lightweight resin-based ablative thermal protection materials under aerodynamic heating, including the microstructure morphology, the lapping relationship of components, and the evolution of components and pores. In addition, there are no public reports on the microstructure evolution and heat transfer modeling of low-density resin-based thermal protection composites with complex microstructure during aerodynamic heating.

So, in this paper, we aim to conduct an in-depth study of the microstructure evolution of resin-based ablative materials under aerodynamic heating. Based on the microstructure, the multiscale unit cell models are established to predict the equivalent thermal conductivity, and the influence of microstructure parameters is also studied.

The research on the mesoscopic heat transfer mechanism and thermal conductivity prediction of composite materials mainly includes the establishment of theoretical model and finite element model.

In terms of theoretical model, the thermal conductivity prediction model of composite materials was first proposed by Maxwell and Rayleigh, which was later modified and improved by scholars to form the thermal conductivity prediction model of composite materials applicable to different situations; the Maxwell model is as follows [13]:

$$\frac{k_{\text{eff}}}{k_m} = 1 + \frac{3\phi}{((k_1 + 2k_m)/(k_1 - k_m)) - \phi}. \quad (1)$$

Here, ϕ is the volume fraction of filled particles, and k_m , k_1 , and k_{eff} are the thermal conductivity of matrix-filled particles and the composite separately. The Maxwell model is

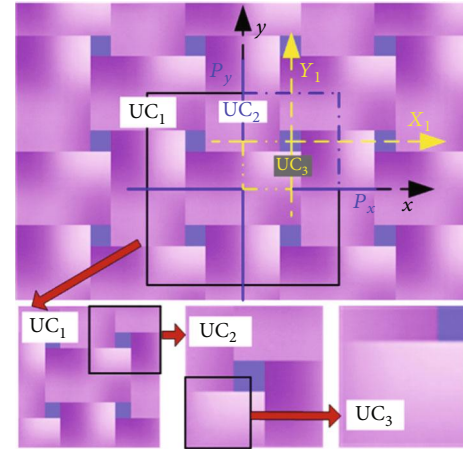


FIGURE 5: Unit cell modeling of braided composites [29].

applicable to materials with particle volume fraction less than 25%; that is, no contact between particles is considered.

Rayleigh considers the cubic arrangement of particle fillings and the thermal interactions between the models, so the model can be used to predict the thermal conductivity of composites with higher particle filling; the Rayleigh model is as follows [14]:

$$\frac{k_{\text{eff}}}{k_m} = 1 + \frac{3\phi}{((k_1 + 2k_m)/(k_1 - k_m)) - \phi + 1.569((k_1 - k_m)/(3k_1 - 4k_m))\phi^{10/3} + \dots}. \quad (2)$$

Hasselman and Johnson [15] took into account the effects of filling size and boundary thermal conductivity and derived the equivalent thermal conductivity expression, respectively, for the composite materials filled with spherical particles, cylindrical fibers, and flat particles, which is called

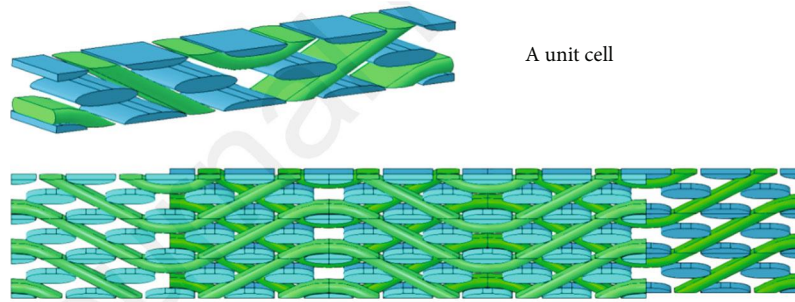


FIGURE 6: Unit cell modeling for parametric analysis of braided composites [33].

the Hasselman-Johnson model. The Benveniste-Miloh model considers the influence of the thermal contact resistance between the filler and matrix [16]. Bruggeman proposed the effective medium theory (EMT) [17]. In 1986, based on EMT and the improved Benveniste-Miloh model, Every et al. proposed the Every model [18], which can predict the thermal conductivity of composites with higher volume filling. In addition, based on the Maxwell model and considering the thermal contact resistance, Nan et al. proposed a thermal conductivity prediction model in 1997 [19].

In addition to the classical thermal conductivity prediction model, in recent years, based on the material microstructure and one-dimensional heat transfer assumption, the thermal resistance series and parallel method has been applied to the thermal conductivity prediction of some composites, such as, polymer-hollow microsphere composite [20], microsphere accumulation composite [21], high-porosity metal foam [22], polymer composite [23], two-phase composite [24, 25], and resin matrix composite [26]; based on one-dimensional heat transfer hypothesis and thermal resistance series and parallel, the expression of equivalent thermal conductivity of composite was derived, which can predict the thermal conductivity of some composites accurately.

With the development of computers and software, the finite element method has been applied in the property prediction of composite materials. The unit cell modeling based on material microstructure and thermal conductivity prediction by finite element method have been developed greatly. In terms of unit cell modeling, Li et al. conducted boundary condition discussion and finite element-based thermal conductivity prediction for unidirectional fiber composites, braided composites, and granular-reinforced composites [27–33] (as shown in Figures 5 and 6). In addition, Zhou et al. [34], Liu et al. [35], and Uhlířová and Pabst [36] also conduct the unit cell modeling and finite element-based thermal conductivity prediction for the microstructure of the composite material and obtain the thermal conductivity prediction result which is close to the experimental result.

However, in terms of microheat transfer mechanism modeling and thermal conductivity prediction of composite materials, most of them focus on materials with relatively simple microstructure, such as unidirectional fiber composites, braided composites, and particle-reinforced composites. For low-density resin-based ablative thermal protection materials with complex microstructure, such as complex

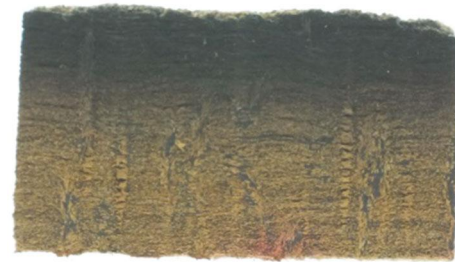


FIGURE 7: Image of material after wind tunnel test.

microstructure materials containing hollow microspheres, fibers, pores, and particles, the heat transfer mechanisms can just focus on the original material [26] or the carbonized material [37]. There are few reports of unit cell modeling and heat transfer characteristic analysis of microstructure evolution.

So, as for the research status of the microstructure evolution and heat transfer characteristics, a typical resin-based ablative material was studied. The multiscale unit cell models were established to get the equivalent thermal conductivity, and the relationship between microstructure evolution and material heat transfer is discussed. The structure of this paper is as follows. Section 2 describes the sample preparation and statistical analysis of microstructure size. Section 3 shows the multiscale unit cell heat transfer modeling and the prediction of thermal conductivity. Analysis of the correlation between microstructure evolution and heat transfer process is shown in Section 4. Section 5 shows some conclusions.

2. Sample Preparation and Statistical Analysis of Microstructure Size

2.1. Sample Preparation. The plate test model of the resin-based ablative material was tested in the ground wind tunnel. The model with surface ablation, middle pyrolysis, and original material was obtained.

Figure 7 is the image of the material evolution process after the wind tunnel test. It is clear that the surface layer of the material is completely pyrolytic, leaving residual carbon. The color of the inner layer becomes lighter, and the pyrolysis ratio becomes smaller until the innermost original material layer.

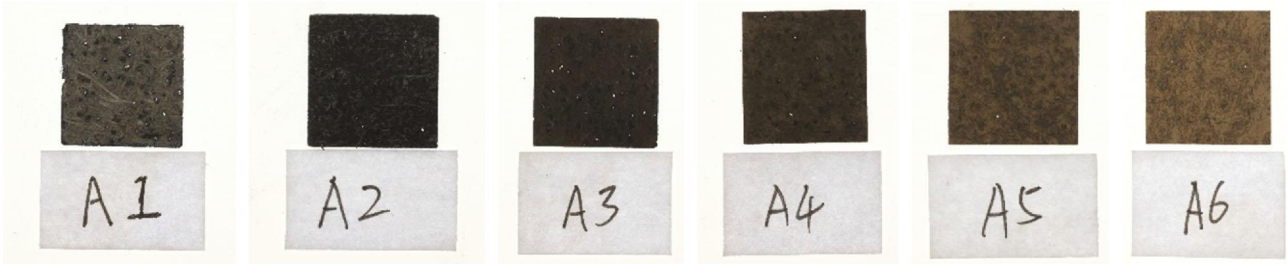


FIGURE 8: Image of material samples at different locations.

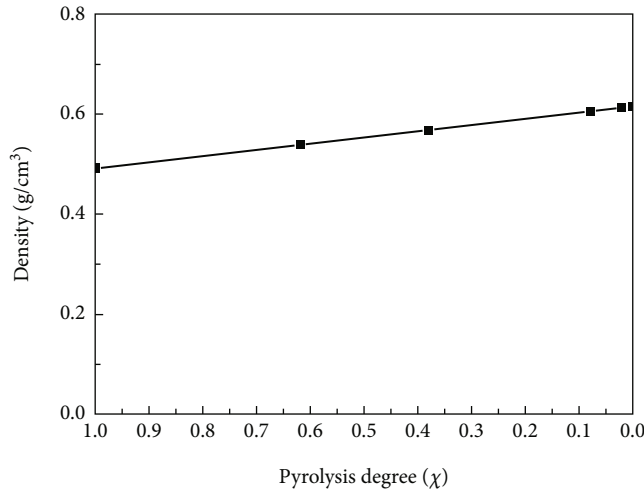


FIGURE 9: Variation of material density with pyrolysis ratio.

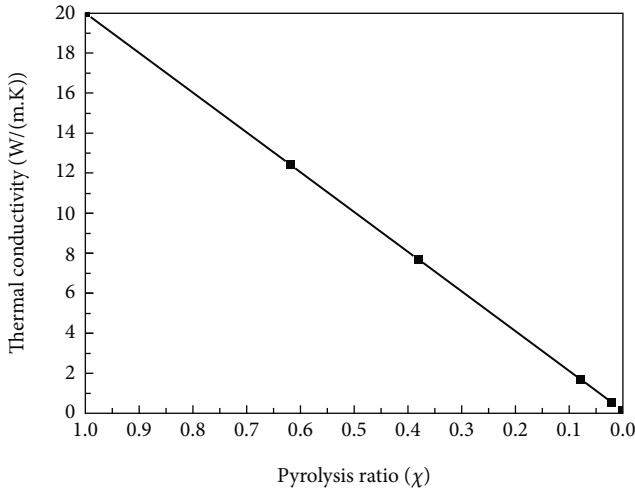


FIGURE 10: Variation of thermal conductivity of phenolic resin matrix with pyrolysis ratio.

TABLE 1: Material composition parameters.

ρ_{fiber} ($\text{g}\cdot\text{cm}^{-3}$)	$\rho_{\text{resin-original}}$ ($\text{g}\cdot\text{cm}^{-3}$)	$\rho_{\text{resin-carbonized}}$ ($\text{g}\cdot\text{cm}^{-3}$)	ρ_{total} ($\text{g}\cdot\text{cm}^{-3}$)	ω_{fiber} (%)	ω_{resin} (%)
2.2	1.1	1.8	0.6	50	50

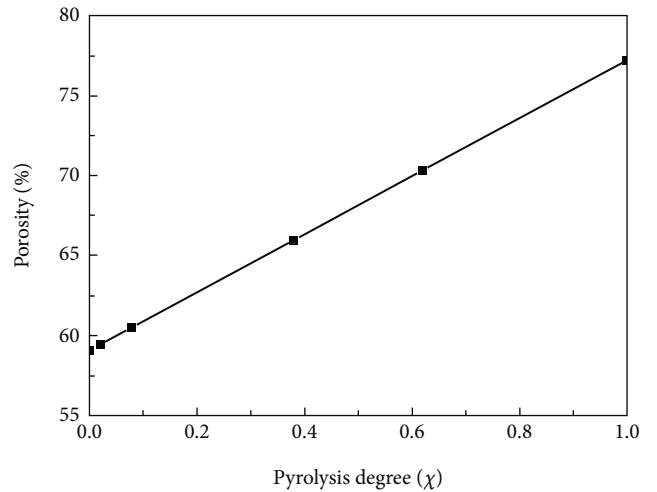


FIGURE 11: Variation of total porosity with pyrolysis ratio.

The length and width of the material samples are 15 mm, and the thickness was the thickness of the model after the wind tunnel test, which was roughly 12 mm. In order to preserve the microstructure morphology of the material to the maximum extent, the wire cutting method was adopted. Starting from the surface of the material, the

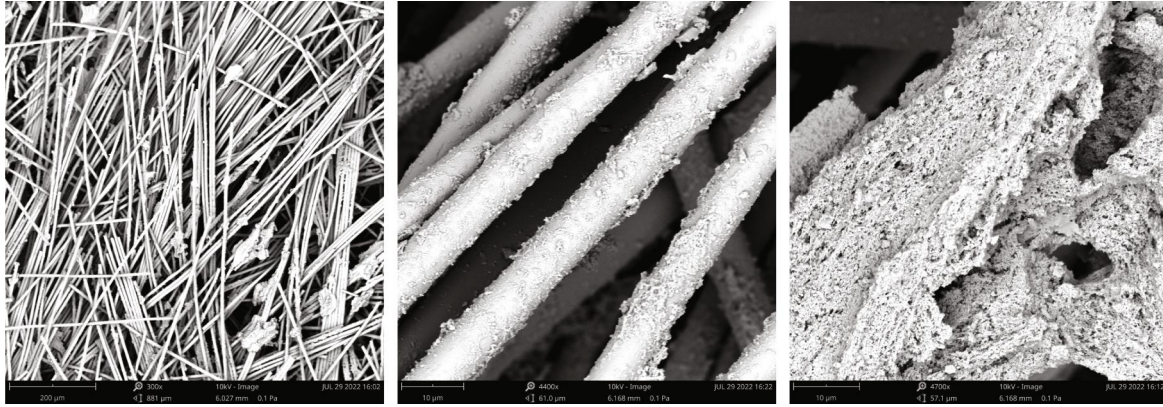


FIGURE 12: Image of surface microstructure of layer A1.



FIGURE 13: Image of surface microstructure of layer A6.

material with a certain thickness was successively cut, and the section numbers were successively A1, A2, A3, A4, A5, and A6. The macropicture of the samples is shown in Figure 8. It can be seen that from the surface to the interior, the color of the sample successively changes from black to light; that is, the carbonization ratio decreases successively, until the interior of the material is the original material.

2.2. Calculation of Pyrolysis Ratio at Different Locations of the Sample. The internal pyrolysis ratio of the material was defined as follows:

$$\chi = \frac{\rho_p - \rho}{\rho_p - \rho_c}. \quad (3)$$

Here, ρ is the current density of the material, ρ_c is the density of the material after complete pyrolysis, and ρ_p is the density of the original material.

Since the samples are a regular rectangle, their density can be obtained by measuring volume and mass, so the pyrolysis ratio of each layer can be calculated using Equa-

tion (3). The material density ranging with pyrolysis ratio is shown in Figure 9. It can be seen that from the surface to the interior, the pyrolysis ratio decreases and the material density increases until it reaches the density of the original material.

2.3. Analysis of Thermal Properties of Phenolic Resin Materials. The main change of resin-based ablative materials in the process of aerodynamic heating is the pyrolysis of phenolic resin. The parallel model is used to obtain the thermal conductivity of phenolic resin matrix changing with the pyrolysis ratio.

$$k_m = k_c \chi + (1 - \chi)k_0. \quad (4)$$

Here, k_c is the thermal conductivity of residual carbon of phenolic resin after carbonization, and it is $k_c = 20 \text{ W}/(\text{m} \cdot \text{K})$. k_0 is the thermal conductivity of phenolic resin, and it is $k_0 = 0.15 \text{ W}/(\text{m} \cdot \text{K})$. The variation of thermal conductivity of matrix with the pyrolysis ratio is shown in Figure 10.

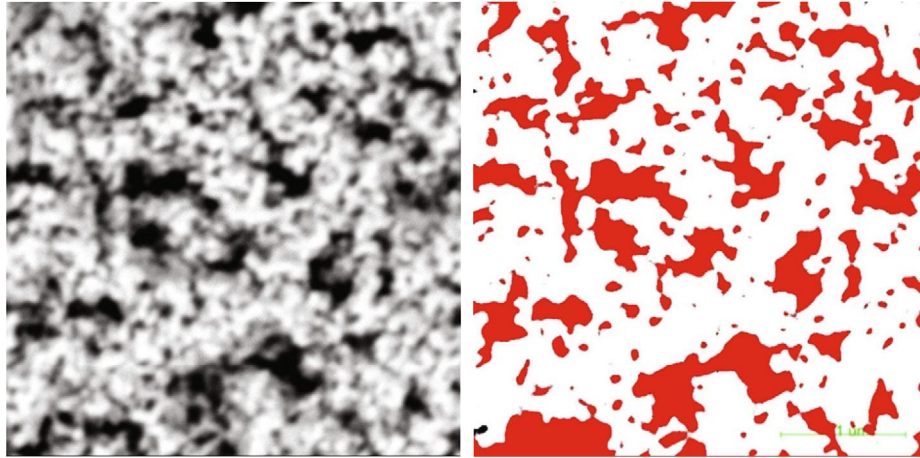


FIGURE 14: Nanoscale pore image and pore label image of layer A1.

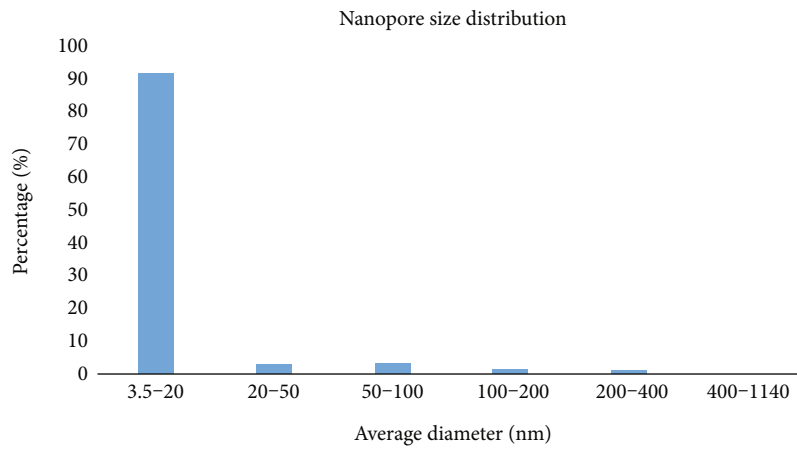


FIGURE 15: Nanoscale pore size distribution of layer A1.

TABLE 2: The nanoscale porosity and pore size distribution of A1 to A6.

	A1	A2	A3	A4	A5	A6
Nanoscale porosity (%)	27.79	27.71	35.45	39.15	31.28	38.64
Pore size distribution (nm)	3.5~20	20	5~20	3~20	2.4~20	6~20



FIGURE 16: Micron-scale pore image and pore labeling map on the back of layer A1.

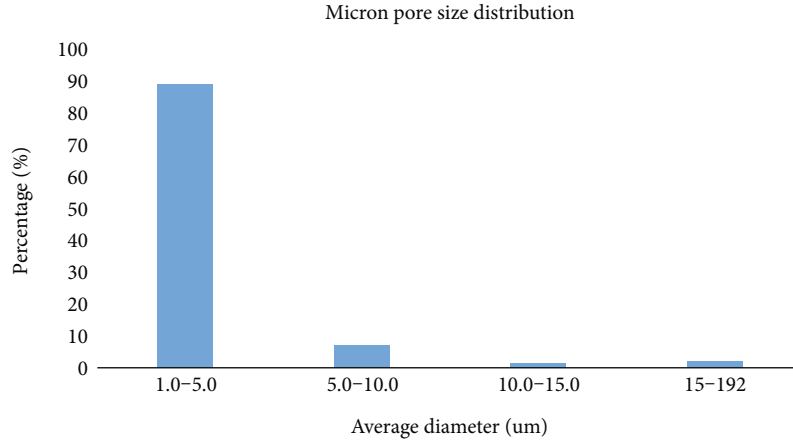


FIGURE 17: Micron-scale pore size distribution of A1 layer.

TABLE 3: The micron-scale porosity and pore size distribution of A1 to A6.

	A1	A2	A3	A4	A5	A6
Microscale porosity (%)	31.9	31.42	32.56	32.43	27.72	26.4
Pore size distribution (μm)	1~5	1~5	1~5	1~5	1~5	1~5

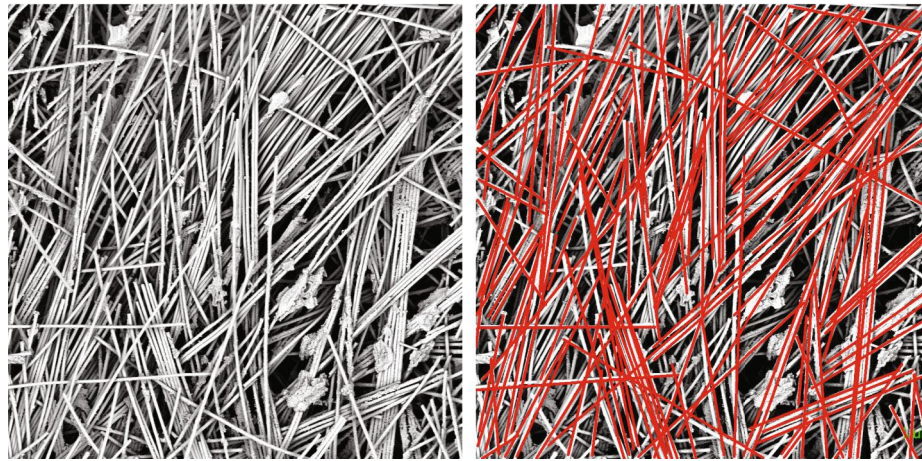


FIGURE 18: Fiber-scale image and fiber length label map.

2.4. Variation Law of Material Total Porosity. The material composition parameters are shown in Table 1. The volume fraction of fiber is

$$\varphi_{\text{fiber}} = \frac{\omega_{\text{fiber}}/\rho_{\text{fiber}}}{1/\rho_{\text{total}}} \times 100\% = 13.6\%. \quad (5)$$

The volume fraction of phenolic resin in original material is

$$\varphi_{\text{resin-original}} = \frac{\omega_{\text{resin}}/\rho_{\text{resin-original}}}{1/\rho_{\text{total}}} \times 100\% = 27.3\%. \quad (6)$$

The porosity factor of original material is

$$\text{porosity}(\chi = 0) = 1 - \varphi_{\text{fiber}} - \varphi_{\text{resin-original}} \times 100\% = 59.1\%. \quad (7)$$

The residual carbon ratio is 55%, and the ratio of volume after carbonization to volume before carbonization is

$$V_{\text{c-o}} = \frac{V_{\text{resin-carbonized}}}{V_{\text{resin-original}}} = 0.55 \times \frac{\rho_{\text{resin-original}}}{\rho_{\text{resin-carbonized}}} \times 100\% = 33.61\%. \quad (8)$$

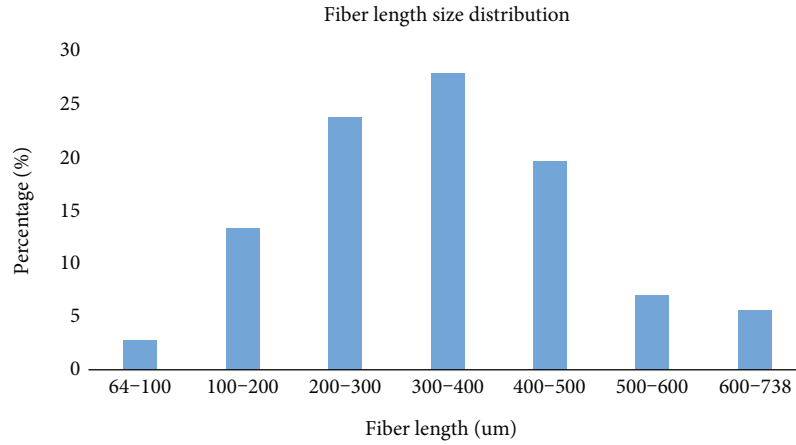


FIGURE 19: Fiber length distribution.

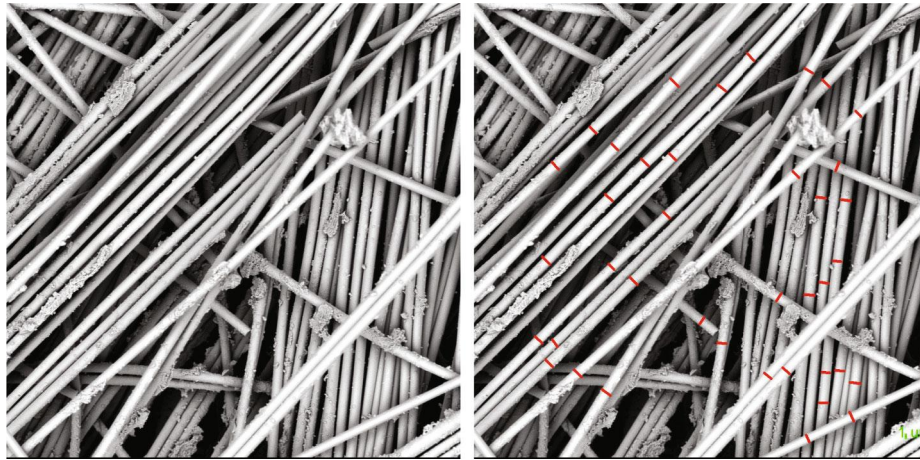


FIGURE 20: Fiber-scale image and fiber diameter label map.

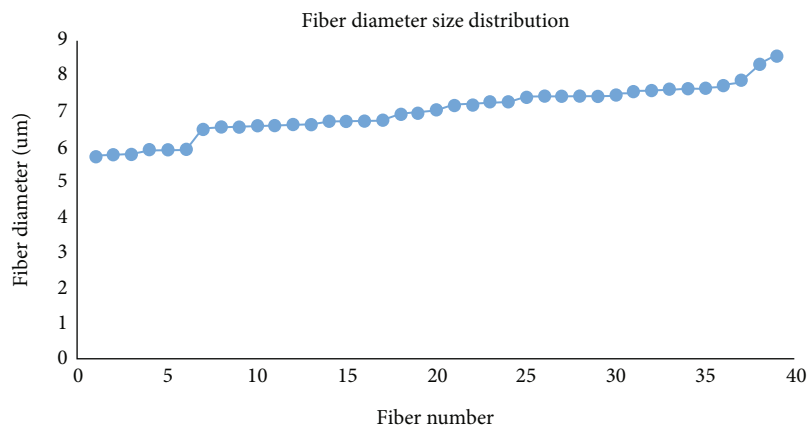


FIGURE 21: Fiber diameter distribution.

The volume fraction of phenolic resin with different pyrolysis ratio is

$$\varphi_{\text{resin}}(\chi) = \varphi_{\text{resin-original}} \cdot \chi \cdot V_{\text{c-o}} + (1 - \chi) \cdot \varphi_{\text{resin-original}} \quad (9)$$

The porosity factor with different pyrolysis ratio is

$$\text{porosity}(\chi) = 1 - \varphi_{\text{resin}}(\chi) - \varphi_{\text{fiber}} \quad (10)$$

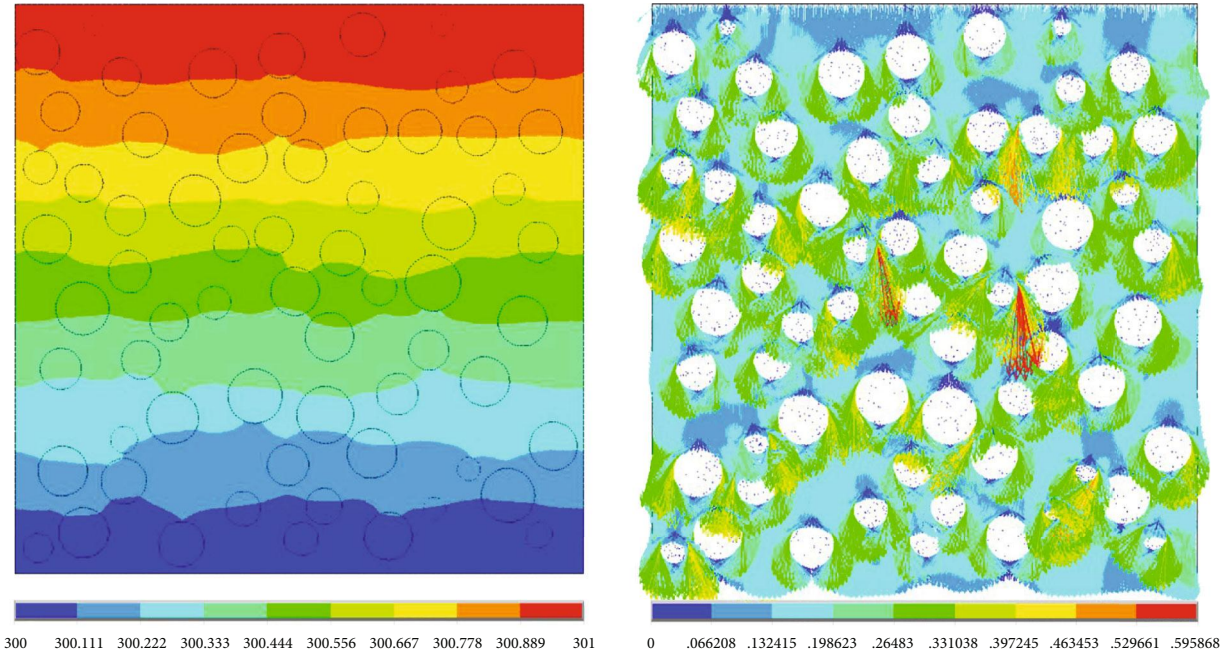


FIGURE 22: Nanoscale pore distribution calculation, temperature cloud map, and heat flow vector map.

So, the porosity factor is shown in Figure 11. With the increase of pyrolysis ratio, the porosity factor of the material increases significantly, which is due to the volume shrinkage during pyrolysis.

2.5. Microstructure Images at Different Stages of Pyrolysis. The samples at different pyrolysis stages were sprayed with gold, and the microstructure was observed by scanning electron microscope. Figure 12 is the surface section, and Figure 13 is the typical microstructure image of the sixth layer section. It indicates that the material is composed of fibers and nanometer resin matrix, and the fibers are arranged in the tiling and z direction. Therefore, the microstructure size statistics are mainly conducted from the size and distribution of nanopores at the matrix scale and the size and distribution of micropores and fibers at the fiber scale. At the matrix scale, the volume content of nanoscale was calculated, and at the fiber scale, the volume content of fiber and micron pores was calculated. Since there are some differences in the microstructure of materials with the same pyrolysis ratio at different locations, the method of measuring three typical microstructure images and taking average values is adopted in the process of microstructure distribution, size, and content statistics.

Figure 12 is the microstructure image of the upper surface of A1, which is the part in contact with aerodynamic heating. The microstructures indicate that most of the material is composed of fibers, the matrix content is small, and only a small part of the matrix is attached to the fibers. The reason is that the residual carbon formed by the pyrolysis resin in the process of aerodynamic heating will undergo oxidation reaction under the condition of aerodynamic heating. In addition, some residual carbon has been subjected to airflow erosion, so the matrix content in the surface material is less.

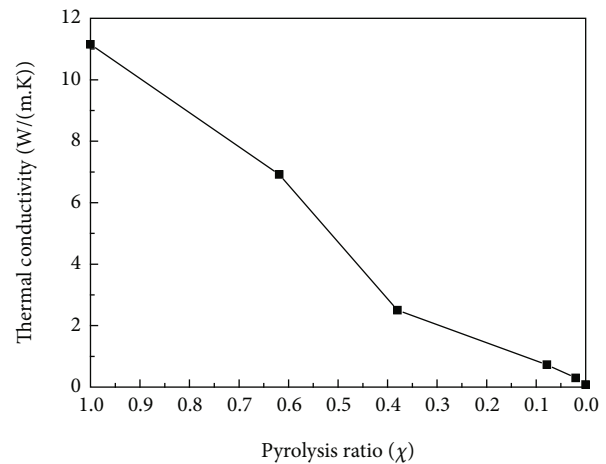


FIGURE 23: Nanoscale equivalent thermal conductivity varies with pyrolysis ratio.

2.6. Distribution of Microstructure Size

2.6.1. Statistics and Analysis of Pore Microstructure Size Distribution. As for the reason that the matrix exists a little on the surface because of airflow erosion and ablation, we take back microstructure of each layer.

(1) Microstructure of Layer A1.

(1) Statistics and distribution of nanopore size

Size statistics were made on the microstructure image of layer A1, we use the software of Image-Pro Plus to label and count the microstructure size and distribution, as shown in

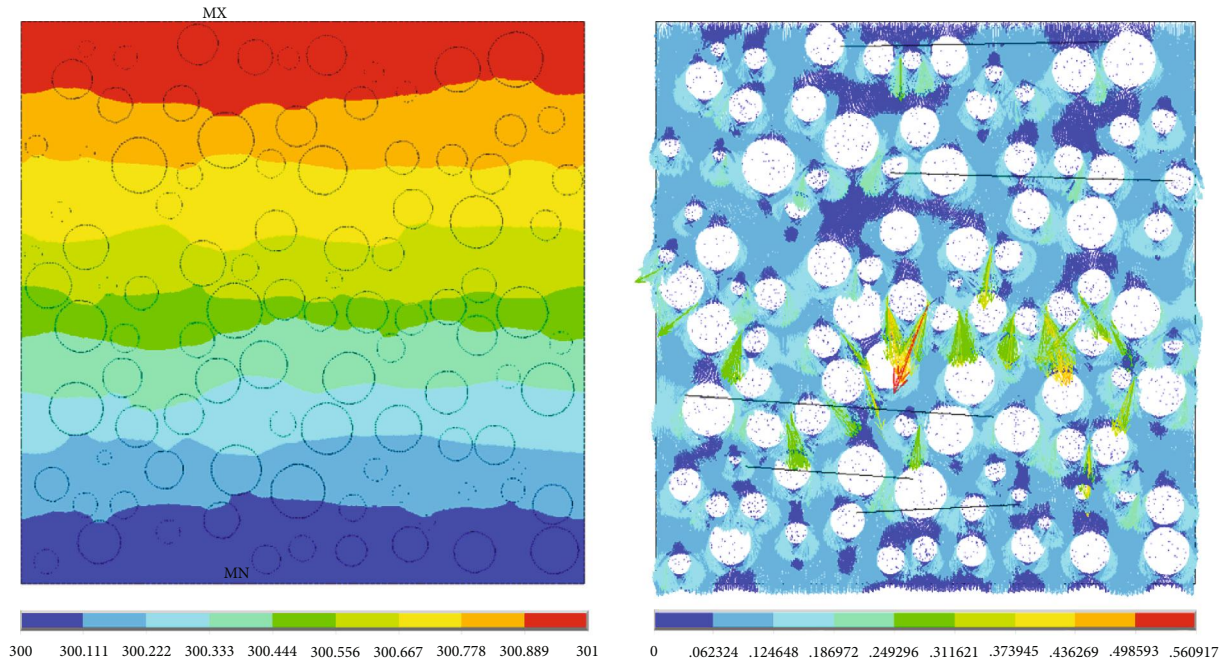


FIGURE 24: Micron-scale temperature cloud and heat flow vector.

Figure 14. The total area of pores and the total area of the image were calculated, and the calculated porosity factor was 27.41%. Figure 15 shows the statistical results of pore size distribution. It indicates that the diameter of most pores is 3.5~20 nm and the number of larger pores is small.

The images of three different positions were taken for statistics, and the average porosity factor was taken. The nanoscale porosity of A1 was 27.72%.

The nanoscale porosity and pore size distribution of A1 to A6 are shown in Table 2.

(2) Statistics and distribution of micron pore size

Size statistics were made on the micron-scale microstructure image of layer A1, as shown in Figure 16. The total area of pores and the total area of the image were calculated, and the calculated porosity was 32.74%. Figure 17 shows the statistical results of pore size distribution. It can be seen that most pores have diameters ranging from 1.0 to 5.0 microns and the number of larger pores is small.

The average porosity of three images at different positions was obtained. The micron-scale porosity of A1 was 31.90%.

The microscale porosity and pore size distribution of A1 to A6 is shown in Table 3.

2.6.2. Statistical Analysis of Fiber Microstructure Size Distribution. As can be seen from the material microstructure image, the quartz fiber does not undergo melting and other changes in the test state, and its morphology does not change during the ablation process. Therefore, the statistical analysis of fiber size is carried out for the microstructure of the surface material with obvious fiber distribution.

Figure 18 is fiber-scale image and fiber length label map. It can be seen that the distribution of fiber length is relatively uniform, ranging from more than 60 microns to 1,000 microns, with little difference in quantity, which is shown in Figure 19. The fiber diameter varies from 5.5 microns to 8.5 microns, and the distribution is relatively uniform, as shown in Figures 20 and 21. Therefore, the length and diameter of the fiber can be considered as a uniform distribution within a certain size range when generating the fiber. The representativeness was increased by means of the average value of the images at different locations.

3. Multiscale Heat Transfer Modeling and Thermal Conductivity Prediction

3.1. Heat Transfer Modeling

3.1.1. Modeling and Equivalent Thermal Conductivity Prediction of Nano-Pore-Scale Cells of Layer A1 (Carbonized Layer). The surface layer is completely carbonized, so the resin matrix is completely transformed into residual carbon. According to the above statistics, the nanoscale porosity is 27.72%, and the average pore diameter is between 0 and 20 nm. The pores have an irregular structure, which is considered as spherical pores. We use the APDL code of Ansys Mechanical software to establish the finite element model.

Skochedopole [38] found in the experiment that for the hole whose diameter was less than 4 mm, there was no natural convection of the gas. The pore size is very small, and its equal diameter is far less than $192 \mu\text{m}$, so we ignore the thermal convection. We focus on the heat transfer characteristics in room temperature, so we also ignore the gas radiation.

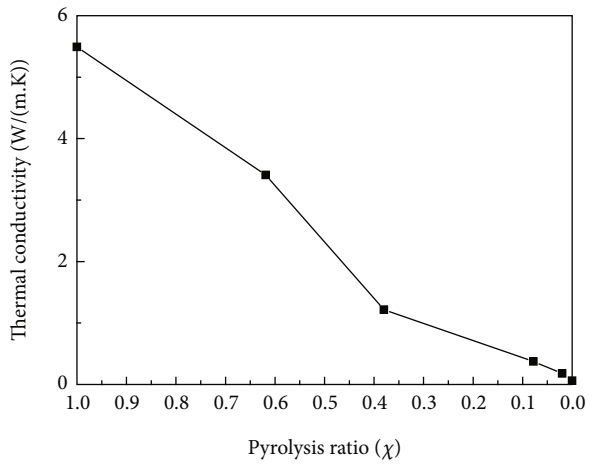


FIGURE 25: The variation of micron equivalent thermal conductivity with pyrolysis ratio.

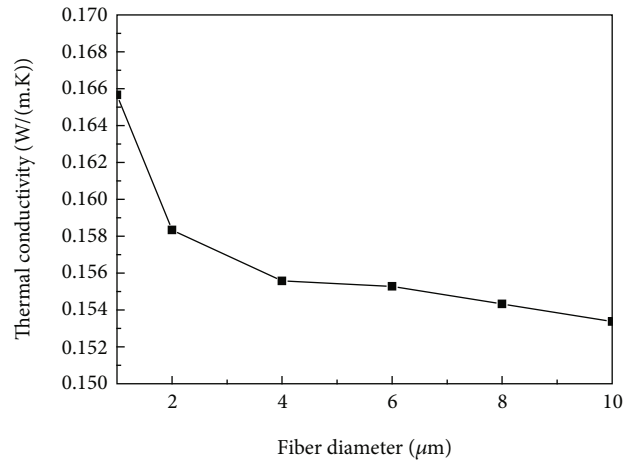


FIGURE 28: The effect of fiber diameter on micron-scale thermal conductivity.

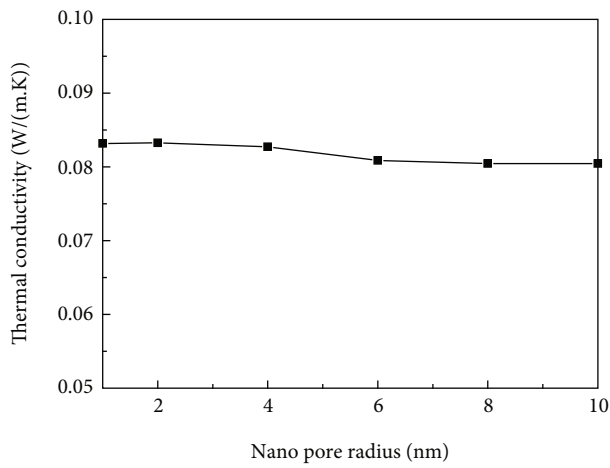


FIGURE 26: Effect of nanopore size on nanoscale thermal conductivity.

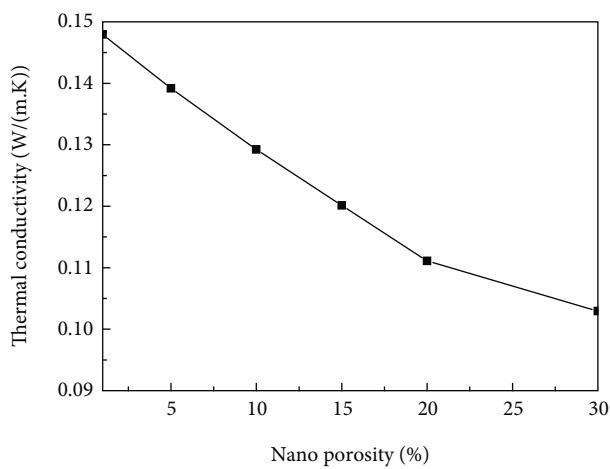


FIGURE 27: Effect of nanoporosity on nanoscale thermal conductivity.



FIGURE 29: Side microstructure image.



FIGURE 30: Top microstructure image.

TABLE 4: Effect of the angle between the normal direction of plane O and the heat transfer direction y on the thermal conductivity in y direction.

Angle (°)	0	30	45	60	90
Thermal conductivity (W/(m·K))	0.0624	0.0706	0.0799	0.0875	0.0995

Periodic boundary conditions and temperature boundary conditions are applied to solve the problem. The size of the unit cell model is $a \times a \times a$, so, the periodic boundary conditions and temperature boundary conditions are show in

$$\begin{aligned} T_{(-a,y,z)} - T_{(a,y,z)} &= 0, \\ T_{(x,y,-a)} - T_{(x,y,a)} &= 0, \end{aligned} \quad (11)$$

$$T_{(x,-a,z)} - T_{(x,a,z)} = 2a\nabla T_y. \quad (12)$$

The heat flux Q flowing along the y direction is acquired. Using Fourier's law shown as Equation (13), we can get the equivalent thermal conductivity shown as Equation (14).

$$Q = kA \frac{\Delta T_y}{a}, \quad (13)$$

$$k = \frac{Q}{a\Delta T_y}. \quad (14)$$

The temperature nephogram and heat flow vector diagram are shown in Figure 22.

3.1.2. Calculation Results of Nanoscale Thermal Conductivity Variation with Pyrolysis Ratio. For the other layers of A2~A6, considering different pyrolysis ratio and physical parameters, the method similar to the previous section is used to calculate the nanoscale thermal conductivity under different pyrolysis ratios, and the results are shown in Figure 23. It can be seen that the equivalent thermal conductivity at the nanoscale increases with the increase of pyrolysis ratio. The reason is that the conductivity of resin matrix increases significantly with pyrolysis ratio.

3.1.3. Micron-Scale Cell Modeling and Equivalent Thermal Conductivity Prediction of Layer A1 (Carbonized Layer). At the micron scale, according to the above statistics, the porosity is 31.9%, the average pore diameter is between 1 and 5 microns, and the pores are irregular structure. Here, they are considered as spherical pores, and the control body is taken as 100-micron meters, and the spherical pores are randomly generated. According to the statistical results of fibers, there is little difference in fiber diameter, so the average value is taken as 7 microns. The fiber volume fraction was calculated to be 13.6% by the composition of material physical parameters, and the fiber was generated according to this proportion. The Boolean operation was carried out, the grid was drawn, periodic boundary conditions and temperature boundary conditions were applied for calculation, and the heat flow through the heat transfer direction was obtained. The predicted results of the thermal conductivity were calculated using the Fourier law. Temperature cloud map and heat flow vector are shown in Figure 24.

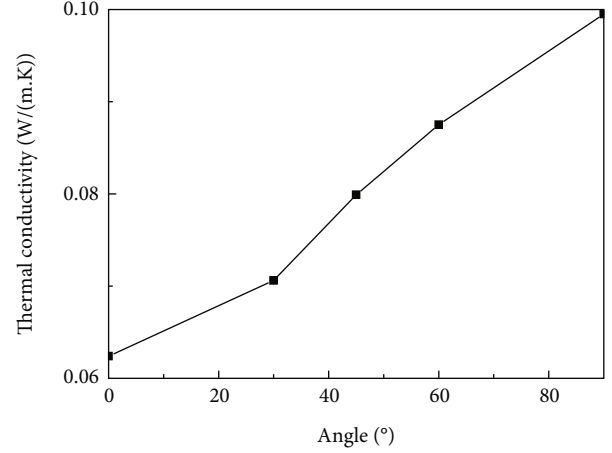


FIGURE 31: Effect of the angle between the normal direction of plane O and the heat transfer direction y on the thermal conductivity in y direction.

3.1.4. Calculation Results of Micron-Scale Thermal Conductivity Variation with Pyrolysis Ratio. Micron-scale thermal conductivity at different pyrolysis ratios was calculated, and the results are shown in Figure 25. It can be seen that the micron-scale equivalent thermal conductivity increased with the increase of pyrolysis ratio. The variation is mainly because of the thermal conductivity in the nanoscale.

3.2. Equivalent Thermal Conductivity Test Verification. The thermal conductivity of the original material at room temperature tested by hot-wire experiment technique is 0.07 W/(m·K) , and the calculated result is 0.061917 W/(m·K) . Therefore, the errors are as follows:

$$\varepsilon = \frac{0.07 - 0.061917}{0.07} \times 100\% = 11.5\%. \quad (15)$$

So, the method of multiscale thermal conductivity prediction is verified by the experiment.

4. Analysis of the Correlation between Microstructure Evolution and Heat Transfer Process

4.1. Influence of Nanoscale Pores. Taking the same porosity, the influence of the change of pore size on the nanoscale thermal conductivity was discussed. Since the model was randomly distributed, the average value was calculated multiple times. The thermal conductivity ranging with the nanoscale pore size is shown in Figure 26. The thermal conductivity varies a little when the nanoscale pore size

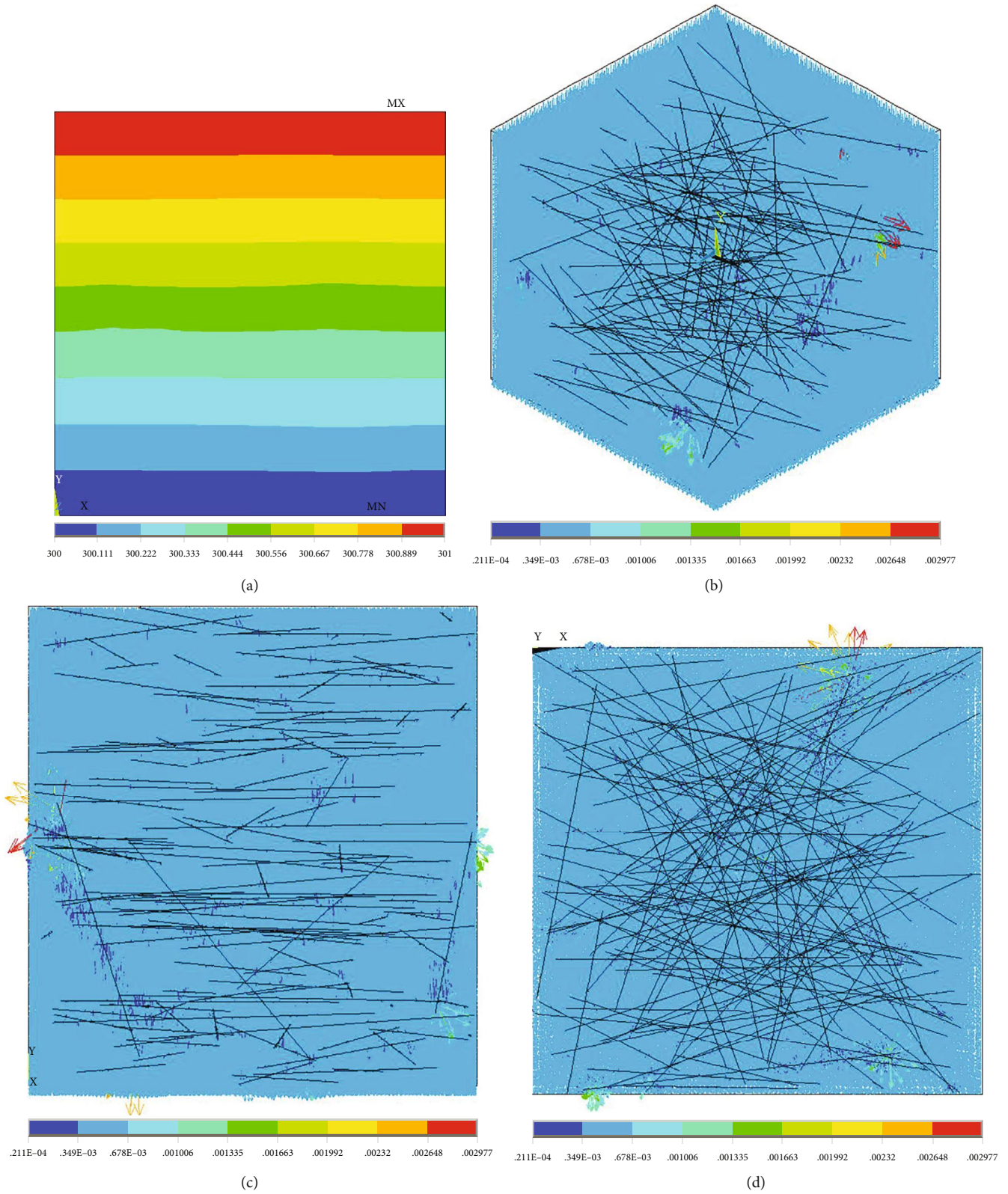
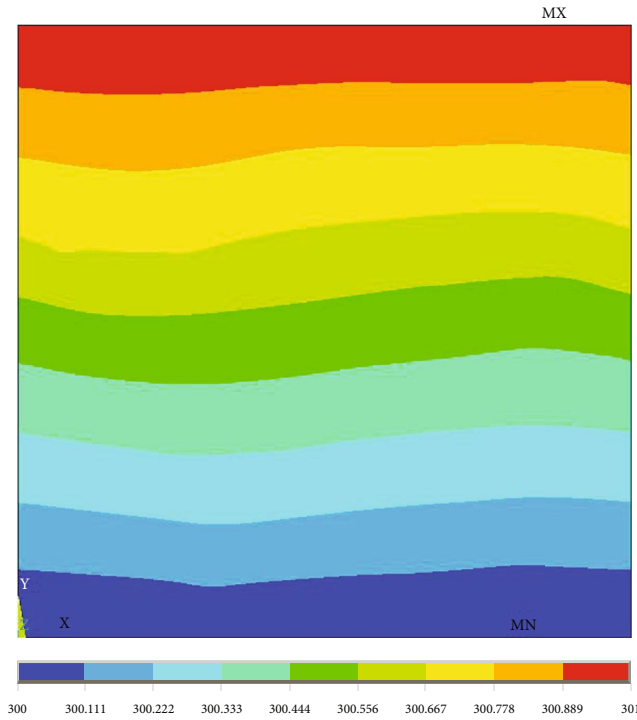


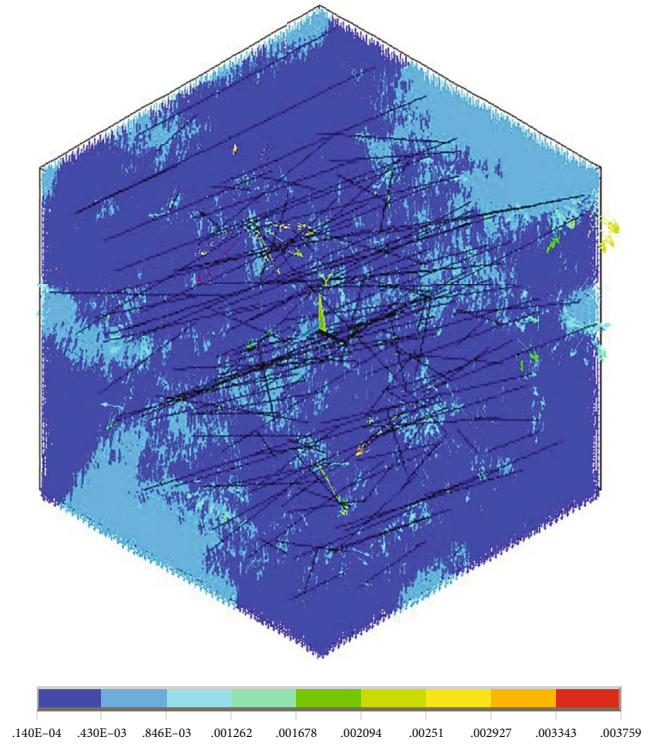
FIGURE 32: 0° temperature cloud and heat flow map. (a) Elevation view of temperature cloud map, (b) axial view of heat flow map, (c) elevation view of heat flow map, and (d) top view of heat flow map.

changes. We can conclude that when the volume fraction is constant, the nanopore size has little effect on the nanoscale thermal conductivity.

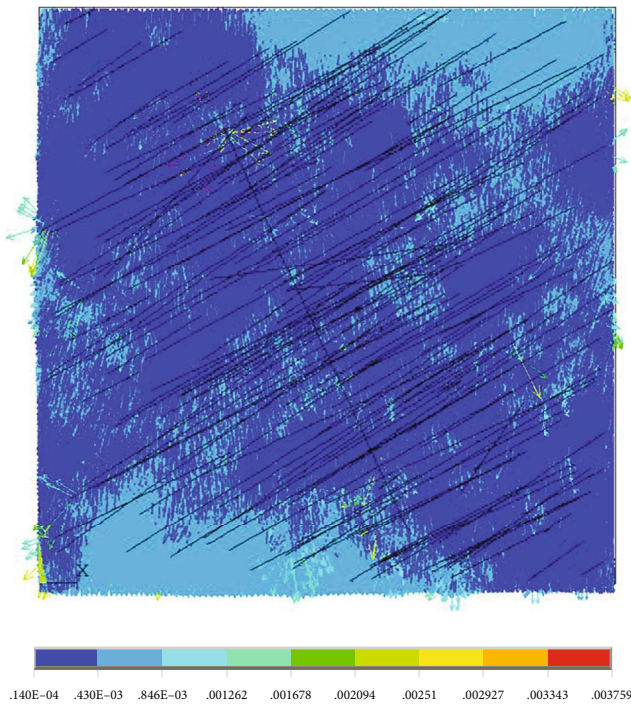
For different nanoporosity, the influence of the porosity on the nanoscale thermal conductivity was calculated, and the result is shown in Figure 27. It can be seen that the



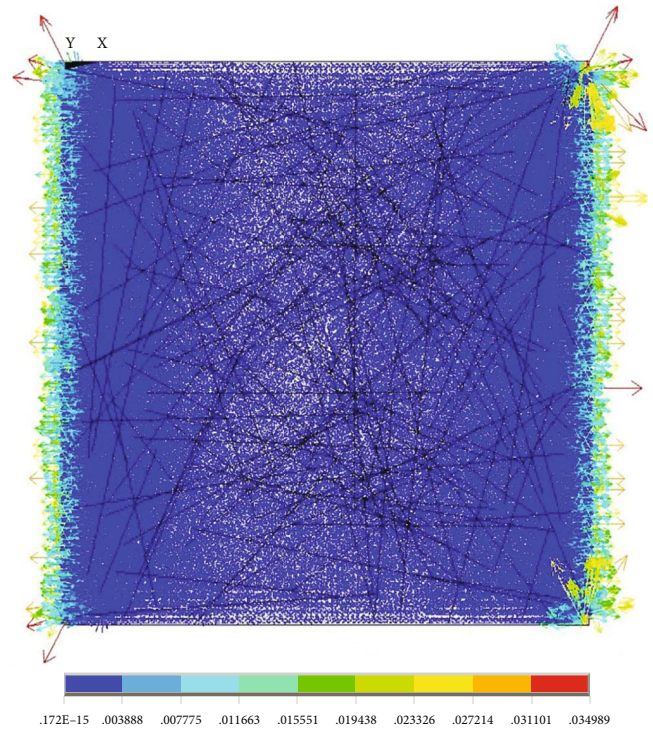
(a)



(b)



(c)



(d)

FIGURE 33: 30° temperature cloud and heat flow map. (a) Elevation view of temperature cloud map, (b) axial view of heat flow map, (c) elevation view of heat flow map, and (d) top view of heat flow map.

nanoscale thermal conductivity decreases with the increase of the porosity. This is because the thermal conductivity of air is low, and the larger porosity will reduce the thermal conductivity of the material.

4.2. *Influence of Fiber Size.* The effect of fiber diameter on micron-scale thermal conductivity is shown in Figure 28. The fiber volume fraction is fixed and the fiber orientation is random, and the fiber-scale equivalent thermal conductivity can

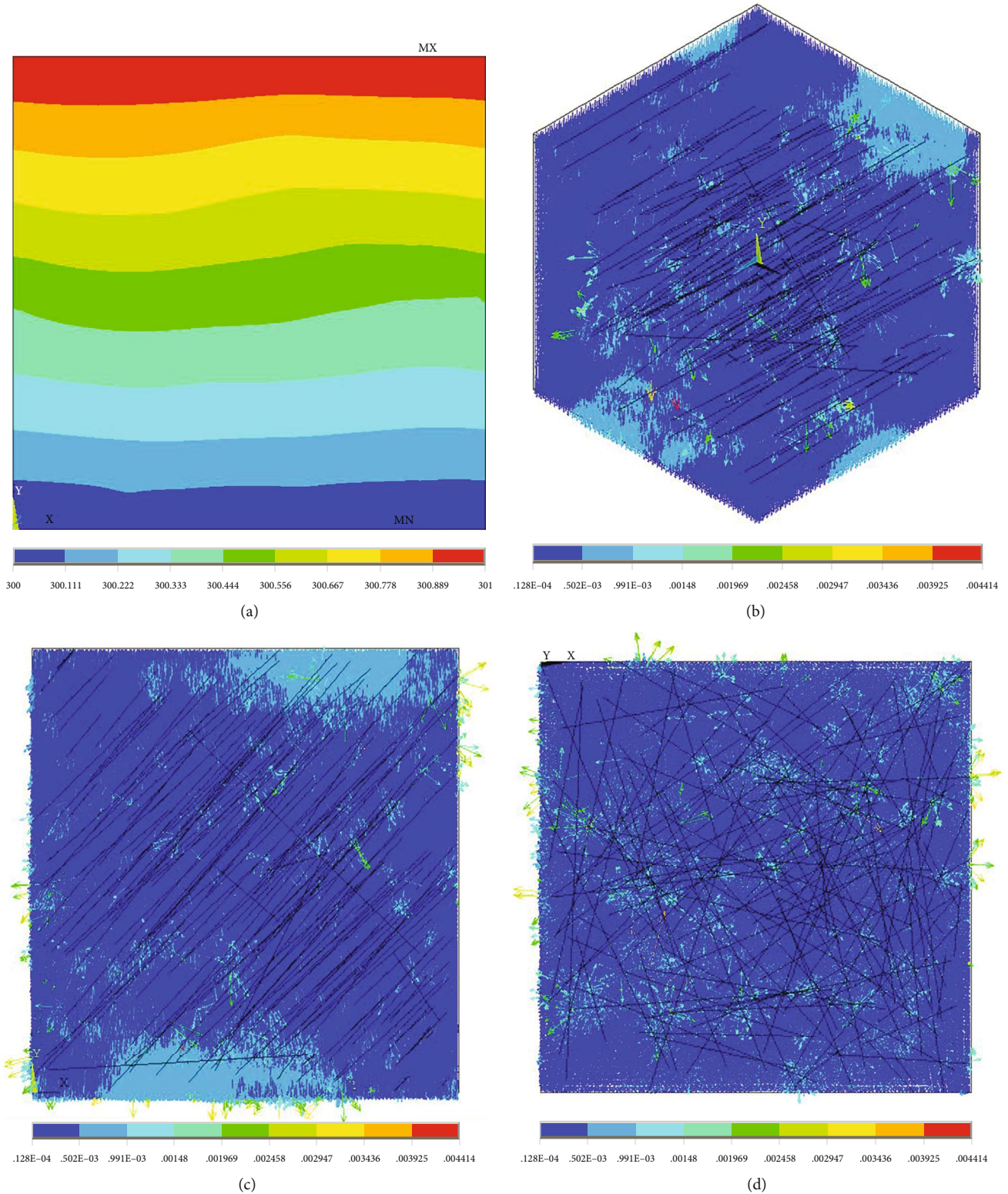
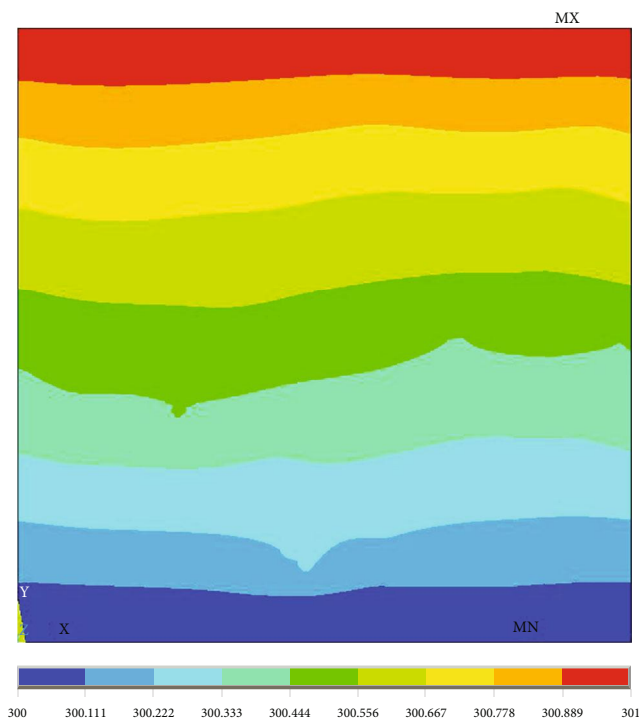


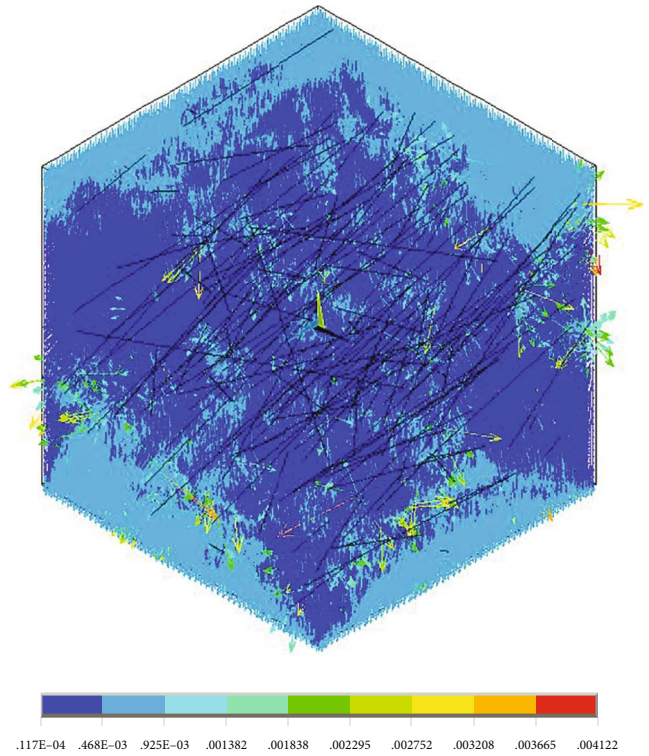
FIGURE 34: 45° temperature cloud and heat flow map. (a) Elevation view of temperature cloud map, (b) axial view of heat flow map, (c) elevation view of heat flow map, and (d) top view of heat flow map.

be calculated by different fiber diameters. It can be seen that the micron-scale equivalent thermal conductivity increases with the fiber diameter. As for the original material, the thermal

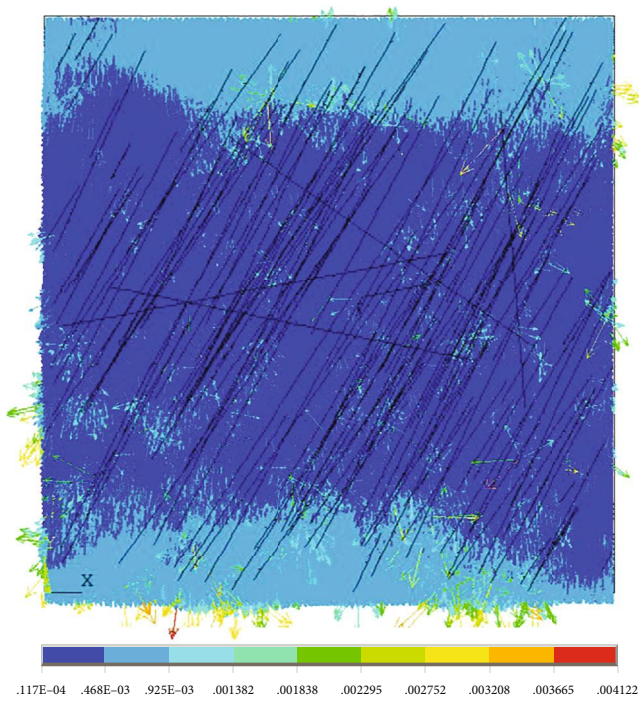
conductivity of fiber is bigger than other constituents, and the bigger fiber leads to a smaller number of fibers. So, the thermal conductivity is smaller with bigger fiber diameter.



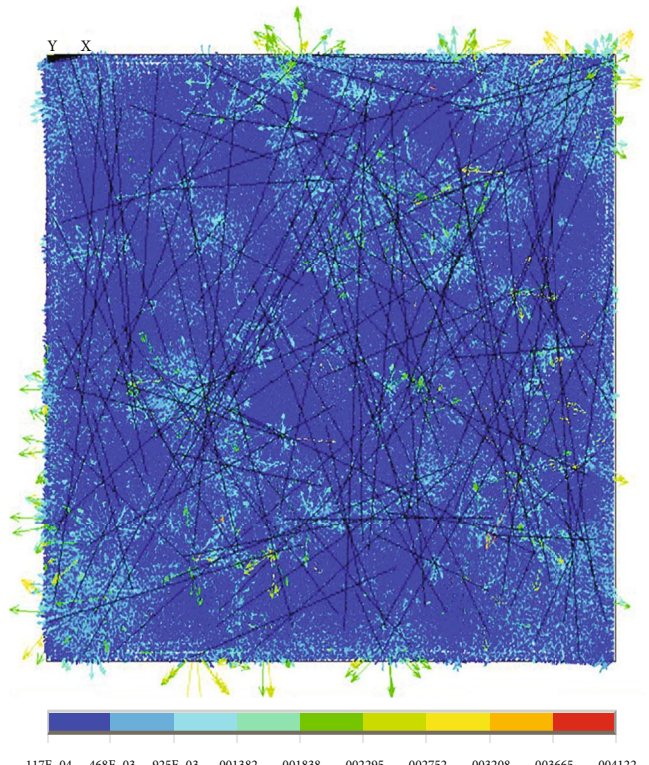
(a)



(b)



(c)



(d)

FIGURE 35: 60° temperature cloud and heat flow map. (a) Elevation view of temperature cloud map, (b) axial view of heat flow map, (c) elevation view of heat flow map, and (d) top view of heat flow map.

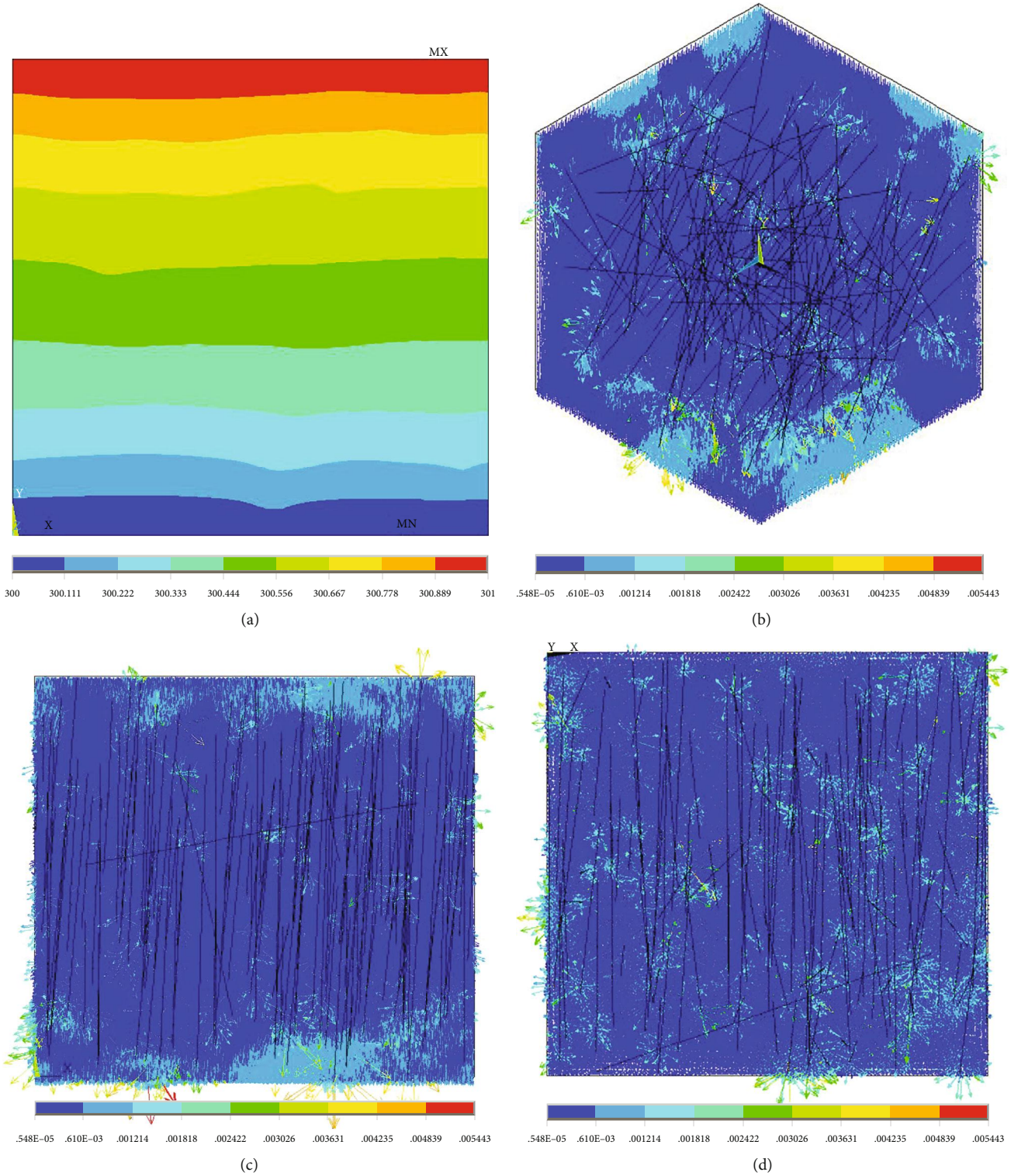


FIGURE 36: 90° temperature cloud and heat flow map. (a) Elevation view of temperature cloud map, (b) axial view of heat flow map, (c) elevation view of heat flow map, and (d) top view of heat flow map.

4.3. Influence of Fiber Anisotropy Distribution on Thermal Conductivity. Figures 29 and 30 show the microstructure images observed on the side and top surfaces, respectively. It can be seen that most fibers are randomly distributed and lay-

ered on the surface which is vertical to the heat transfer direction, and a small number of fibers are roughly distributed along the heat transfer direction. The influence of fiber orientation change on the thermal conductivity is discussed below.

Fiber randomly distributed in plane O. The angle between the normal direction of plane O and the heat transfer direction is 90 degrees in the actual material of this paper. The thermal conductivity results of the material are discussed below when the normal direction of plane O and the heat transfer direction are, respectively, at an angle of 0°, 30°, 45°, 60°, and 90°.

Here, the original material parameters of the material were taken as the research object, and the equivalent thermal conductivity was obtained by modeling the microstructure of the resin and nanopores first. Then, the equivalent thermal conductivity of the micron pores and the matrix was obtained by taking the thermal conductivity as the input, and the thermal conductivity of the new matrix was 0.060773 W/(m·K). The obtained equivalent thermal conductivity at different angles between the normal direction of plane O and the heat transfer direction γ is shown in Table 4 and Figure 31, and the temperature cloud and heat flow diagram are shown in Figures 32–36. We can see that the thermal conductivity is larger when the orientation of fiber is the same with the heat transfer direction.

5. Conclusion

In this paper, based on the slicing, weighing, size measurement, microstructure observation, microstructure size statistics, microstructure modeling, and heat transfer characteristic analysis of resin-based thermal protection material samples at different positions after wind tunnel test, the evolution of microstructure and material physical property parameters at different positions of materials under aerodynamic heating condition was obtained, and the prediction results of material thermal conductivity were obtained. We can see that, from the surface to the interior of the material, the pyrolysis ratio gradually decreases and the material density gradually increases. The predicted thermal conductivity of the material increases with the increase of the pyrolysis ratio. The results show that pore sizes have little influence on the thermal conductivity, while porosity, fiber size, and fiber orientation have great influence on the thermal conductivity. The thermal conductivity decreases with increasing porosity. For fibers, the more fibers along the heat transfer direction, the greater the thermal conductivity is.

Data Availability

Research data supporting this publication are available by contacting the author at gao58_jj@163.com.

Conflicts of Interest

The authors declare that they have no affiliation with or involvement in any organization or entity with any financial interest in the subject matter or materials discussed in this manuscript.

Acknowledgments

We acknowledge the support from the National Natural Science Foundation Committee (Joint Fund Project U20B2017).

References

- [1] G. Jiang and L. Liu, *High Speed Airflow Heat Transfer and Ablative Heat Protection*, National Defense Industry Press, Beijing, 2003.
- [2] S. Han, S. Meng, W. Xie, and Q. Lv, "Hypersonic vehicle \"golden bell jar\",", *China High-tech*, vol. 10, pp. 15–17, 2019.
- [3] B. Ai, *Computational Aerodynamics of Near Space Hypersonic Vehicles*, Science Press, Beijing, 2020.
- [4] Y. Guo, W. Shi, and D. Lei Zeng Baihe, *Theory and Application of Ablative Heat Protection for Hypersonic Vehicles*, Science Press, Beijing, 2019.
- [5] T. H. Ko, W. S. Kuo, and Y. H. Chang, "Raman study of the microstructure changes of phenolic resin during pyrolysis," *Polymer Composites*, vol. 21, no. 5, pp. 745–750, 2000.
- [6] S. S. Tzeng and Y. G. Chr, "Evolution of microstructure and properties of phenolic resin-based carbon/carbon composites during pyrolysis," *Materials Chemistry & Physics*, vol. 73, no. 2-3, pp. 162–169, 2002.
- [7] A. S. Alex, S. Bhuvaneswari, C. Sarath Chandran, T. Jayalatha, and V. Sekkar, "Microstructure and phase evolution in pyrolysed short fibre reinforced polymethylsilsesquioxane-phenolic interpenetrating networks," *Journal of Analytical & Applied Pyrolysis*, vol. 129, pp. 241–247, 2018.
- [8] B. Santhosh, E. Lonescu, F. Andreolli et al., "Effect of pyrolysis temperature on the microstructure and thermal conductivity of polymer-derived monolithic and porous SiC ceramics," *Journal of the European Ceramic Society*, vol. 41, no. 2, pp. 1151–1162, 2021.
- [9] Z. Wang, L. Gao, Y. Ding et al., "Microstructure observation and analysis of 3D carbon fiber reinforced SiC-based composites fabricated through filler enhanced polymer infiltration and pyrolysis," *Ceramics International*, vol. 38, no. 1, pp. 535–540, 2012.
- [10] R. Chen, J. Qi, X. Guo et al., "Surface morphology and microstructure evolution of B4C ceramic hollow microspheres prepared by wet coating method on a pyrolysis substrate," *Ceramics International*, vol. 45, no. 6, pp. 7916–7922, 2019.
- [11] W. Zhang, Q. Ma, K. Zeng, and W. Mao, "Microstructure and properties evolution of C/mullite composites during fabrication process," *Ceramics International*, vol. 47, no. 5, pp. 6623–6632, 2021.
- [12] F. Dong, Q. Ren, R. Hongqian, W. Wang, S. Ren, and C. Zhang, "Mechanical properties and microstructure evolution of SiC ceramics prepared from the purified powders," *Materials Science and Engineering: A*, vol. 802, article 140443, 2021.
- [13] J. C. Maxwell, *A Treatise on Electricity and Magnetism, Vol. I*, Oxford University Press, 3rd edition, 1904.
- [14] R. B. Bird, W. E. Stewart, and E. N. Lightfoot, *Transport Phenomena*, John Wiley & Sons, 2007.
- [15] D. P. H. Hasselman and L. F. Johnson, "Effective thermal conductivity of composites with interfacial thermal barrier resistance," *Journal of Composite Materials*, vol. 21, no. 6, pp. 508–515, 1987.

- [16] Y. Benveniste, "Effective thermal conductivity of composites with a thermal contact resistance between the constituents: nondilute case," *Journal of Applied Physics*, vol. 61, no. 8, pp. 2840–2843, 1987.
- [17] D. A. G. Bruggeman, "Berechnung verschiedener physikalischer konstanten von heterogenen substanzen," *Annalen der Physik*, vol. 416, no. 7, pp. 636–664, 1935.
- [18] A. G. Every, Y. Tzou, D. P. H. Hasselman, and R. Raj, "The effect of particle size on the thermal conductivity of ZnS/diamond composites," *Acta Metallurgica et Materialia*, vol. 40, no. 1, pp. 123–129, 1992.
- [19] C. W. Nan, R. Birringer, D. R. Clarke, and H. Gleiter, "Effective thermal conductivity of particulate composites with interfacial thermal resistance," *Journal of Applied Physics*, vol. 81, no. 10, pp. 6692–6699, 1997.
- [20] F. Li, *Study on Heat Transfer Performance and Mechanism of Polymer/Hollow Microsphere Composites*, South China University of Technology, Guangzhou, 2003.
- [21] W. V. Antwerpen, P. G. Rousseau, and C. G. D. Toit, "Multi-sphere unit cell model to calculate the effective thermal conductivity in packed pebble beds of mono-sized spheres," *Nuclear Engineering & Design*, vol. 247, pp. 183–201, 2012.
- [22] X. H. Yang, J. J. Kuang, T. J. Lu, F. S. Han, and T. Kim, "A simplistic analytical unit cell based model for the effective thermal conductivity of high porosity open-cell metal foams," *Journal of Physics D: Applied Physics*, vol. 46, no. 25, article 255302, 2013.
- [23] A. Agrawal and A. Satapathy, "Mathematical model for evaluating effective thermal conductivity of polymer composites with hybrid fillers," *International Journal of Thermal Sciences*, vol. 89, pp. 203–209, 2015.
- [24] S. Chidambara Raja, L. A. Kumaraswamidhas, P. Karthikeyan, and M. Ramu, "Prediction of pressure dependent effective thermal conductivity of two phase materials in high temperature applications-an analytical method using hexagon and octagon models," *International Journal of Thermal Sciences*, vol. 135, pp. 192–205, 2019.
- [25] V. R. Singh and N. Netam, "Effect of convective heat transfer coefficient on estimation of effective thermal conductivity of two-phase material," *Materials Today: Proceedings*, vol. 28, pp. 2236–2240, 2020.
- [26] J. Gao, J. Yu, H. Han, and D. Deng, "Prediction of mesoscopic heat transfer characteristics of resin-based ablative materials," *Acta Aeronautica et Astronautica Sinica*, vol. 38, Supplement 1, pp. 171–178, 2017.
- [27] H. Li, S. Li, and Y. Wang, "Prediction of effective thermal conductivities of woven fabric composites using unit cells at multiple length scales," *Journal of Materials Research*, vol. 26, no. 3, pp. 384–394, 2011.
- [28] J. J. Gou, H. Zhang, Y. J. Dai, S. Li, and W. Q. Tao, "Numerical prediction of effective thermal conductivities of 3D four-directional braided composites," *Composite Structures*, vol. 125, pp. 499–508, 2015.
- [29] J. J. Gou, Y. J. Dai, S. Li, and W. Q. Tao, "Numerical study of effective thermal conductivities of plain woven composites by unit cells of different sizes," *International Journal of Heat and Mass Transfer*, vol. 91, pp. 829–840, 2015.
- [30] J. J. Gou, W. Z. Fang, Y. J. Dai, and W. Q. Tao, "Multi-size unit cells to predict effective thermal conductivities of 3D four-directional braided composites," *Composite Structures*, vol. 163, pp. 152–167, 2017.
- [31] J.-J. Gou, C.-L. Gong, and W.-Q. Tao, "Appropriate utilization of the unit cell method in thermal calculation of composites," *Applied Thermal Engineering*, vol. 139, pp. 295–306, 2018.
- [32] J. J. Gou, X. J. Ren, W. Z. Fang, S. Li, and W. Q. Tao, "Two small unit cell models for prediction of thermal properties of 8-harness satin woven pierced composites," *Composites Part B: Engineering*, vol. 135, pp. 218–231, 2018.
- [33] M. Xu, E. Sitnikova, and S. Li, "Unification and parameterisation of 2D and 3D weaves and the formulation of a unit cell for composites made of such preforms," *Composites Part A Applied Science and Manufacturing*, vol. 133, article 105868, 2020.
- [34] L. C. Zhou, X. H. Sun, M. W. Chen, Y. B. Zhu, and W. HengAn, "Multiscale modeling and theoretical prediction for the thermal conductivity of porous plain-woven carbonized silica/phenolic composites," *Composite Structures*, vol. 215, pp. 278–288, 2019.
- [35] Y. Liu, Z. G. Qu, J. Guo, and X. M. Zhao, "Numerical study on effective thermal conductivities of plain woven C/SiC composites with considering pores in interlaced woven yarns," *International Journal of Heat and Mass Transfer*, vol. 140, pp. 410–419, 2019.
- [36] T. Uhlířová and W. Pabst, "Thermal conductivity and Young's modulus of cubic-cell metamaterials," *Ceramics International*, vol. 45, no. 1, pp. 954–962, 2019.
- [37] J. Gao, J. Yu, H. Han, and D. Deng, "Prediction of heat transfer characteristics of the carbonized layer of resin-based ablative material based on the finite element method," *International Journal of Aerospace Engineering*, vol. 2019, Article ID 8142532, 14 pages, 2019.
- [38] R. E. Skochdopole, "The thermal conductivity of foam plastics," *Engineering Progress*, vol. 57, pp. 55–59, 1961.